N6-methyladenosine (m^6A) depletion regulates pluripotency exit by activating signaling pathways in embryonic stem cells

Kang-Xuan Jin[a,b,1], Rujuan Zuo[a,1], Konstantinos Anastassiadis[c], Arne Klungland[b,d], Carsten Marr[e,2], and Adam Filipczyk[a,2]

[a]Laboratory for Stem Cell Dynamics, Department of Microbiology, Division of Laboratory Medicine, Oslo University Hospital, Rikshospitalet, Oslo 4950, Norway; [b]Department of Molecular Medicine, Institute of Basic Medical Sciences, University of Oslo, Oslo 1072, Norway; [c]Stem Cell Engineering, Biotechnology Centre, Technische Universität Dresden, 01307 Dresden, Germany; [d]Laboratory for Dynamic Gene Regulation, Department of Microbiology, Division of Laboratory Medicine, Oslo University Hospital, Rikshospitalet, Oslo 4950, Norway; and [e]Institute of Computational Biology, Helmholtz Zentrum München–German Research Centre for Environmental Health, 85764 Neuherberg, Germany

Edited by Frank McCormick, Helen Diller Family Comprehensive Cancer Center, University of California, San Francisco, CA; received March 31, 2021; accepted November 02, 2021

N6-methyladenosine (m^6A) deposition on messenger RNA (mRNA) controls embryonic stem cell (ESC) fate by regulating the mRNA stabilities of pluripotency and lineage transcription factors (TFs) [P. J. Batista et al., *Cell Stem Cell* 15, 707–719 (2014); Y. Wang et al., *Nat. Cell Biol.* 16, 191–198 (2014); and S. Geula et al., *Science* 347, 1002–1006 (2015)]. If the mRNAs of these two TF groups become stabilized, it remains unclear how the pluripotency or lineage commitment decision is implemented. We performed noninvasive quantification of Nanog and Oct4 TF protein levels in reporter ESCs to define cell-state dynamics at single-cell resolution. Long-term single-cell tracking shows that immediate m^6A depletion by Mettl3 knock-down in serum/leukemia inhibitory factor supports both pluripotency maintenance and its departure. This is mediated by differential and opposing signaling pathways. Increased FGF5 mRNA stability activates pErk, leading to Nanog down-regulation. FGF5-mediated coactivation of pAkt reenforces Nanog expression. In formative stem cells poised toward differentiation, m^6A depletion activates both pErk and pAkt, increasing the propensity for mesendodermal lineage induction. Stable m^6A depletion by Mettl3 knock-out also promotes pErk activation. Higher pErk counteracts the pluripotency exit delay exhibited by stably m^6A-depleted cells upon differentiation. At single-cell resolution, we illustrate that decreasing m^6A abundances activates pErk and pAkt-signaling, regulating pluripotency departure.

m^6A | pluripotency | formative stem cells | signaling | single-cell resolution

Pluripotency is governed by a TF regulatory network centered on Oct4, Sox2, and Nanog (1–7). The loss of Oct4, Sox2, and Nanog is a hallmark of pluripotency exit. Although, conventional mouse embryonic stem cell (mESC) culture in serum and leukemia inhibitory factor (LIF) (8, 9) permits cells to undergo a reversible step toward differentiation, marked by the down-regulation of Nanog (10–12). LIF sustains pluripotency through Jak-Stat and PI3K-pAkt signaling pathways acting in parallel (13). In serum-free conditions, LIF and Wnt activation alongside Mek-pErk inhibition enable the capture of mESCs in a pluripotent ground state (14, 15). This homogeneous population represents the newly formed epiblast of the preimplantation mouse embryo (16).

Pluripotency exit involves a formative conversion related to prestreak epiblast in which competence for both soma and germline induction is acquired (17, 18). This was first shown in a transient cell population termed epiblast-like cells (EpiLCs), induced in FGF2 and activin-supplemented, serum-free medium (19). Currently, a lower activin concentration, endogenous FGF-signaling, and inhibition of Wnt and retinoic acid pathways allows the isolation of formative stem (FS) cells (20). These retain the capacity for both soma and germline induction and can be expanded long-term (20). Finally, prolonged culture in high concentrations of FGF2, activin, and inhibition of Wnt-signaling originally allowed the capture of primed pluripotency. Termed epiblast-derived stem cells (EpiSCs) (21), these are refractory to germ cell lineage induction and show relatedness to primed epiblast of the anterior primitive streak (22, 23).

Recently, N6-methyladenosine (m^6A), the most abundant messenger RNA (mRNA) modification (24–26), was shown to be pivotal in pluripotent state regulation (27–29). The Mettl3–Mettl14–Wtap writer complex processes adenosine to m^6A on mRNA (30, 31). Two demethylases, Alkbh5 and FTO, facilitate methylation erasure (32, 33), suggesting that m^6A abundances are reversible and dynamic in nature. Stable m^6A depletion by Mettl3 knock-out (KO) rendered ground-state mESCs poorly responsive to differentiation (28, 29). Increased transcript stability of pluripotency TFs like Nanog is thought to prevent pluripotency network disassembly (24, 28, 29, 34). However, immediate m^6A depletion by Mettl3 knock-down (KD) was reported to differentiate mESCs

Significance

Dynamic deposition of the N6-methyladenosine (m^6A) modification on messenger RNA (mRNA) regulates pluripotency in embryonic stem cells. Reports show that depletion of m^6A abundances increases the mRNA stability of pluripotency and lineage transcription factors (TFs) alike. If the mRNAs of these two TF groups become stabilized, it remains unclear how the pluripotency or lineage commitment decision is implemented. Quantification of pluripotency TFs live at single-cell resolution over generations shows long-term preservation of both pluripotency and priming. m^6A depletion activates key signaling pathways involved in pluripotency versus commitment decisions. This occurs independently of m^6A control over TF mRNA transcript stability. m^6A deposition regulates TF protein expression levels by activating pErk and pAkt signaling to enact cell-fate determination in pluripotent stem cells.

Author contributions: A.F. designed and supervised research; K.-X.J. and R.Z. performed research; K.A. and C.M. contributed new reagents/analytic tools; K.A., A.K., C.M., and A.F. analyzed data; A.F. wrote the paper; and A.F. acquired funding.

The authors declare no competing interest.

This article is a PNAS Direct Submission.

[1]K.-X.J. and R.Z. contributed equally to this work.

[2]To whom correspondence may be addressed. Email: carsten.marr@helmholtz-muenchen.de or dr.adam.filipczyk@gmail.com.

This article contains supporting information online at http://www.pnas.org/lookup/suppl/doi:10.1073/pnas.2105192118/-/DCSupplemental.

Published December 17, 2021.

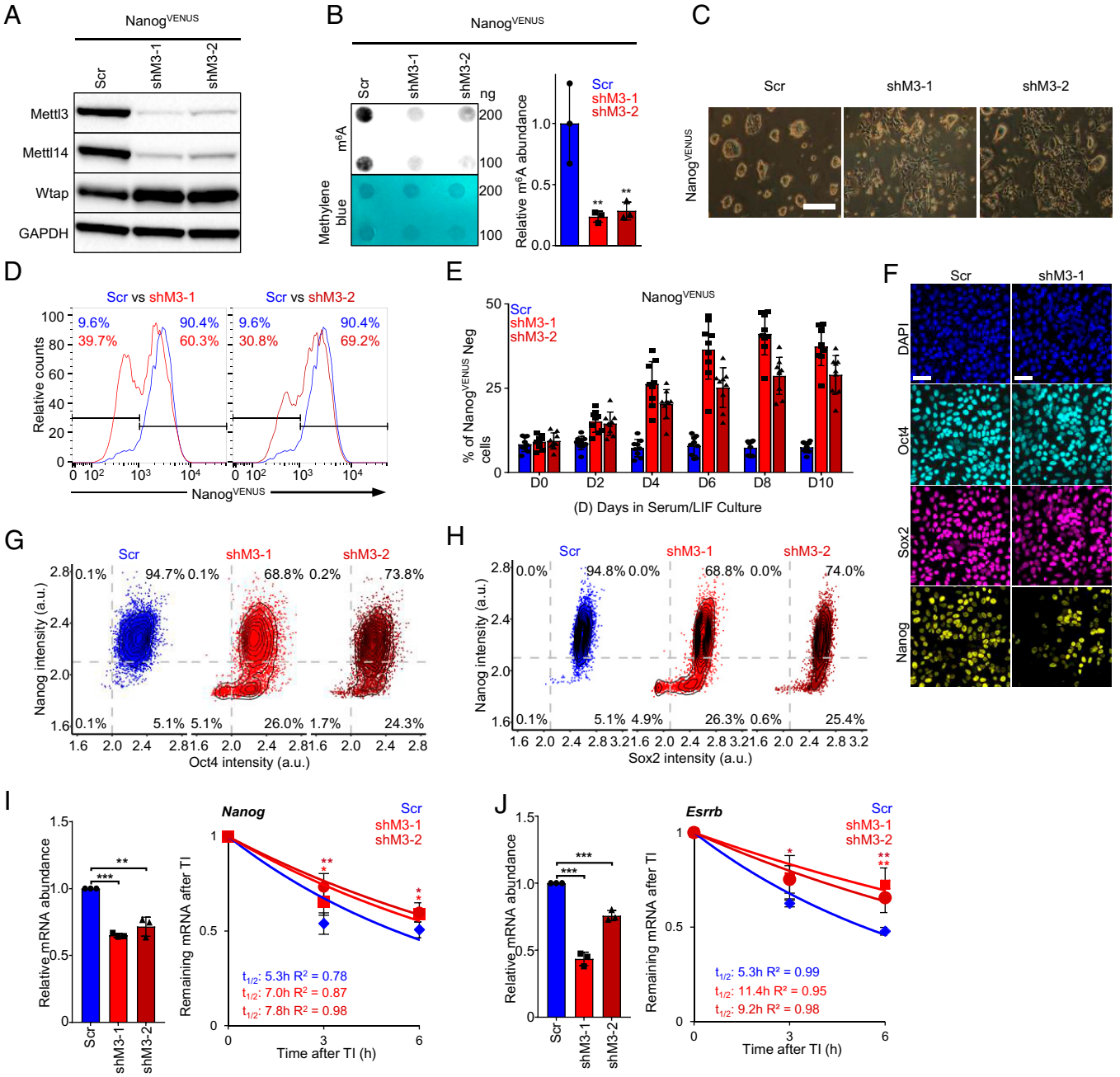

Fig. 1. Immediate m^{6}A depletion promotes Nanog-state heterogeneity in mESCs. (*A*–*J*) mESCs were transduced with control shRNA (Scr) or shRNAs targeting *Mettl3* (shM3-1 and shM3-2). (*A*) Mettl3, Mettl14, and Wtap immunoblots. GAPDH is a loading control. (*B*) Reduction in m6A levels on mRNA upon Mettl3 KD by m6A dot blot (*Left*) and quantification (*Right*). Methylene blue is a loading control. (*C*) Mettl3 KD resulted in flatter colony morphology in NanogVENUS mESCs. (Scale bars, 100 μm.) (*D*) Flow cytometric analysis of Nanog^{VENUS}-negative and -positive cell percentages upon Mettl3 KD in Nanog^{VENUS} mESCs. "Relative counts" indicates normalized cell counts as cumulative percentages up to 100%. (*E*) Proportions of Nanog^{VENUS}-negative cells upon Mettl3 KD, as quantified by flow cytometry using $n = 9$ independent repeats. (*F*) Representative immunostaining for Oct4 (cyan), Sox2 (magenta), Nanog (yellow), and DAPI (blue, cell nuclei) for Scr and shM3-1 cells. (Scale bars, 50 μm.) (*G* and *H*) Multispectral quantitative analysis of immunostaining in *F*. Scatter plot showing fluorescence intensity per cell in arbitrary units (a.u.) for Oct4 versus Nanog (*G*) and Sox2 versus Nanog (*H*). Dashed gray lines mark electronic gates (*Methods*) delineating positive and negative cells. Contour lines indicate probability distribution. Percentages of cells in each compartment are annotated. Analysis of $n = 6{,}239$ (Scr), $n = 5{,}169$ (shM3-1), and $n = 5{,}257$ (shM3-2) cells. (*I* and *J*) Relative mRNA levels (*Left*) and mRNA half-lives (*Right*) for Nanog (*I*) and Esrrb (*J*) in control and m6A-depleted mESCs. mRNA lifetime was determined by monitoring transcript abundance after transcription inhibition (TI), detailed in *Methods*. All statistics include error bars indicating mean ± SD and were calculated using two-tailed independent *t* test and unequal variance, $*P < 0.1$, $**P < 0.05$, and $***P < 0.01$. (*A*) $n = 3$ (*B*), $n = 9$ (*D*), $n = 3$ (*F*–*H*), and $n = 3$ (*I* and *J*) independent repeats. Unless stated otherwise, Nanog^{VENUS} cells were used for experiments and analyzed 10 d after transductions.

grown in Serum/LIF (27, 35) and also EpiSCs (29). These converse effects are attributed to the increased transcript stability of lineage TFs like Otx2 (27). Models suggest that dynamic m^{6}A deposition can create opportune timing for pluripotency or lineage TF mRNAs to become more prevalent over one another and resolve cell fate (24–26, 34, 36). However, questions remain

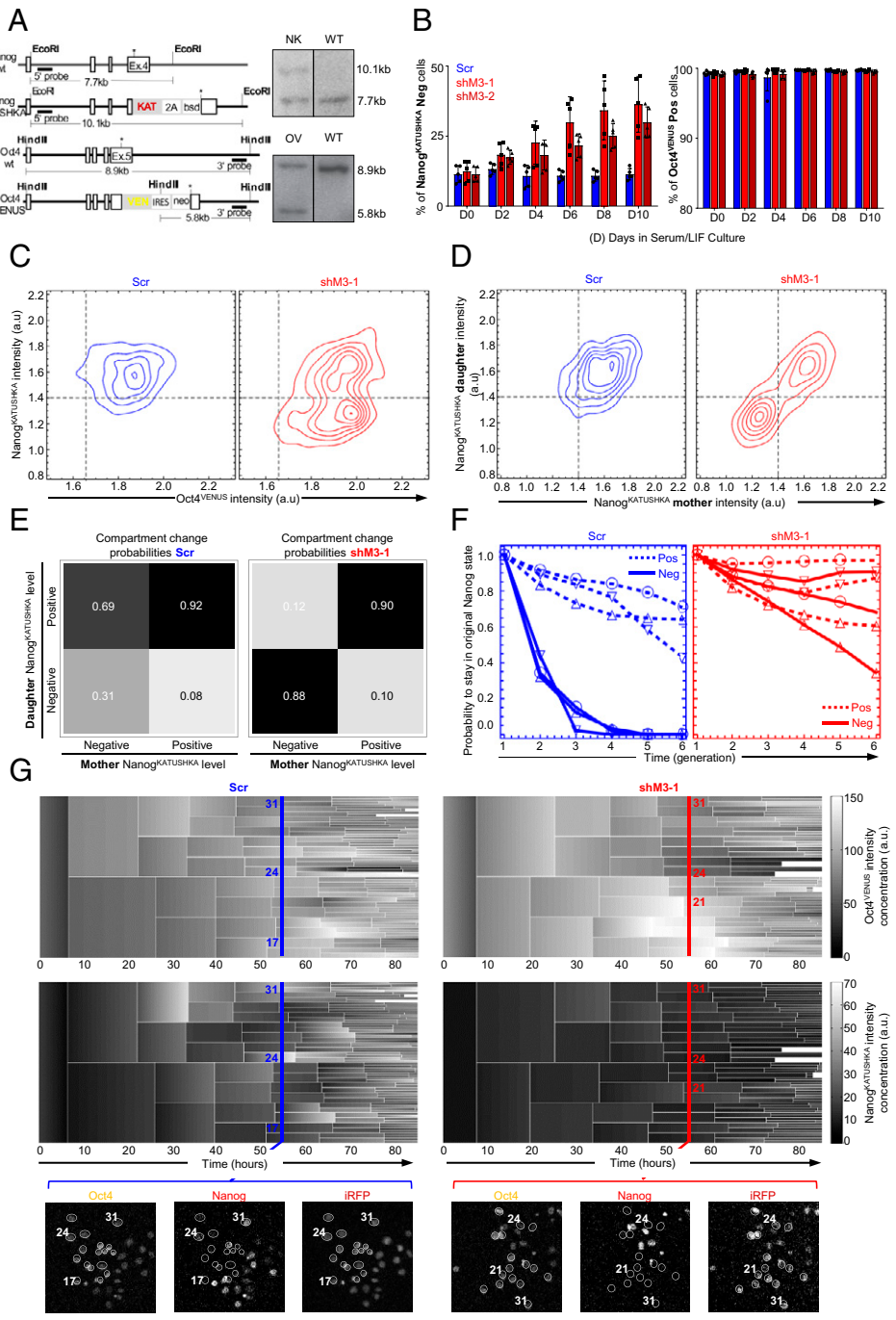

Fig. 2. m^{6}A depletion sustains Nanog-positive and -negative state accumulation. (*A*) Targeting strategy for Nanog^{KATUSHKA}/Oct4^{VENUS} double knock-in reporter mESCs. White rectangles denote exons, and asterisks denote stop codons. Southern blotting verified correct targeting of FPs to the C termini of Nanog and Oct4; NK: Nanog^{KATUSHKA}, OV: Oct4^{VENUS}, and WT: wild-type. (*B*) Cells were transduced with control shRNA (Scr) or shRNAs targeting *Mettl3* (shM3-1 and shM3-2). Proportions of Nanog^{KATUSHKA}-negative (*Left*) and Oct4^{VENUS}-positive (*Right*) cells upon Mettl3 KD as measured by flow cytometry. Error bars indicate mean ± SD from $n = 5$ independent repeats. (*C*–*G*) Cells were transduced with Scr or shM3-1. (*C*) Representative contour plots showing the intensity of Nanog^{KATUSHKA} against Oct4^{VENUS} in a representative live-cell imaging experiment. Cell cycle–corrected intensity data (*Methods*) is shown. (*D*) Transition kernels showing Nanog intensity transitions within one generation between mother and daughter cells. Contour lines indicate the probability distribution of all mother-to-daughter transitions. Representative data showing 844 (Scr) and 956 (shM3-1) mother-to-daughter transitions. (*E*) Positive and negative compartment probability matrices summarize the probabilities for all four types of mother-to-daughter intensity transitions. (In total, 3,058 [Scr] and 3,231 [shM3-1] transitions were analyzed from three independent experiments). (*F*) Nanog^{KATUSHKA}-positive and -negative compartment exit dynamics over time. Dotted and solid lines denote Nanog^{KATUSHKA}-positive and -negative cells, respectively. Each line shows an independent experiment. (*G*) Representative heat trees of Nanog^{KATUSHKA}/Oct4^{VENUS} FP levels in single cells over many cell generations. Each square denotes a cell, and gray scale intensity shows the concentration of Oct4VENUS or Nanog^{KATUSHKA} intensity (*Methods*) for a representative Scr or shM3-1 cell lineage. Colonies from Nanog^{KATUSHKA}-negative founder cells were observed for up to 85 h. At time point 55 h, representative live-cell imaging is shown. White circles denote cell nuclei. Numbered nuclei correspond to numbered cells in the heat tree. The iRFP channel denotes nucmem-iRFP, a constitutively expressed nuclear membrane marker C-terminally fused to the iRFP713 FP. Nucmem-iRFP was engineered into all lentiviral shRNA constructs and used to delineate nuclear area. a.u.: arbitrary unit. All live-cell imaging experiments were performed on Nanog^{KATUSHKA}/Oct4^{VENUS} reporter mESCs with three independent experimental repeats.

whether TF mRNA stability mechanisms negotiate cell fate alone (24, 25) or ensure efficient transcriptome switching once cell-fate choice is established (24, 25).

Current snapshot, population average approaches offer a wealth of information on m^{6}A modification landscapes. They also provide a comprehensive understanding of biochemical processes underlying epi-transcriptomic regulation (24–26, 34, 36). However, only long-term TF quantification at single-cell resolution enables the precise deconvolution of m^{6}A-dependent cell-fate decisions. To this end, we developed transgenic mESC lines to quantify multiple pluripotency TF protein levels in live cells over many generations (11). Over half-a-million time-resolved data points from more than 8,000 cells reveal that m^{6}A depletion supports pluripotency heterogeneity. Importantly, m^{6}A depletion activates pErk- and pAkt-signaling pathways facilitating both pluripotency maintenance and its departure.

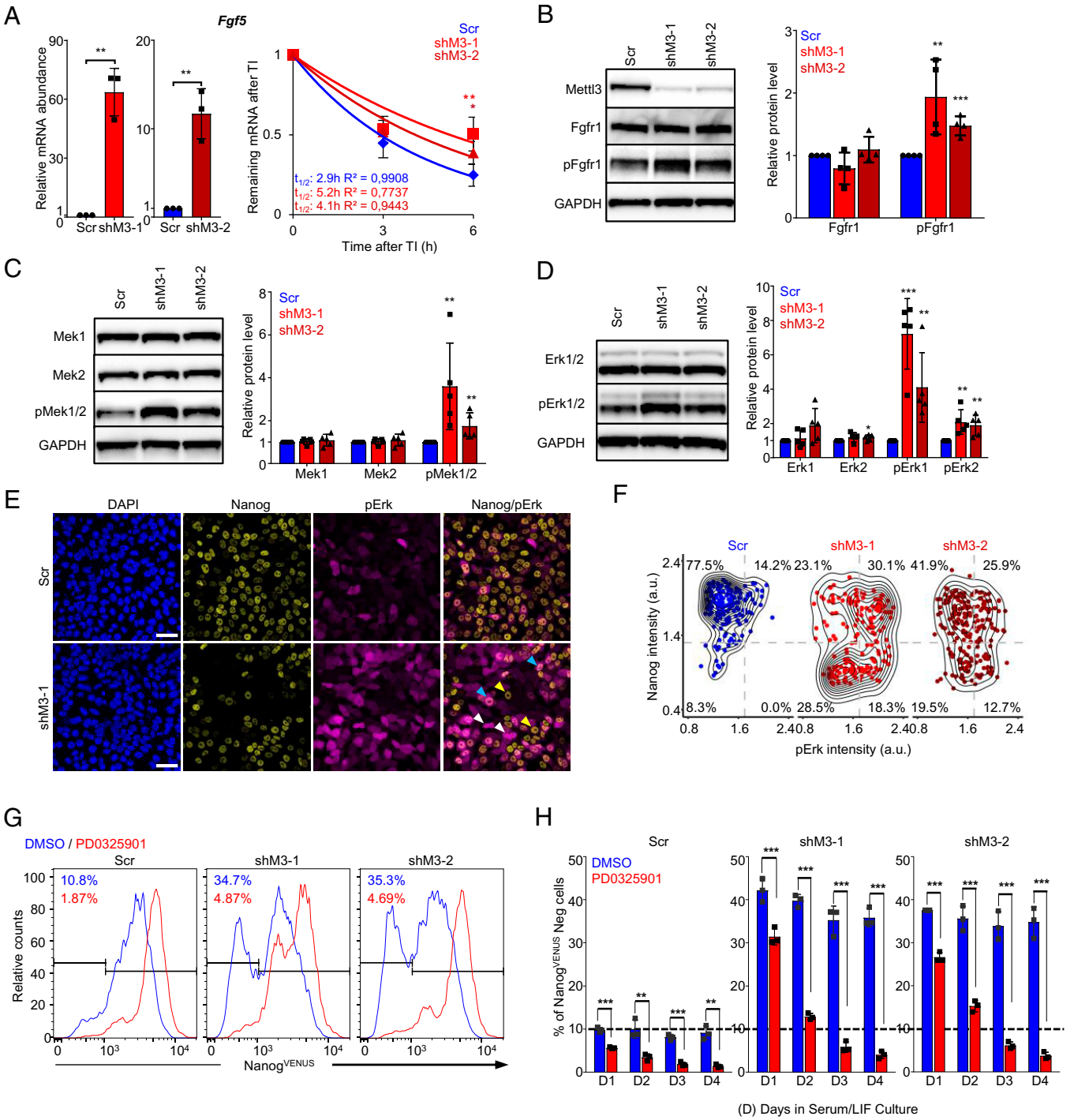

Fig. 3. m^{6}A depletion activates Mek-pErk promoting Nanog-negative state accumulation. (*A–H*) mESCs were transduced with control shRNA (Scr) or shRNAs targeting *Mettl3* (shM3-1 and shM3-2). (*A*) Relative mRNA level (*Left*) and mRNA half-life (*Right*) for *Fgf5*. (*B*) Immunoblot for total Fgfr1 and phosphorylated Fgfr1 (pFgfr1). Quantification of immunoblot shown on the right. (*C* and *D*) Immunoblot for total Mek1/2 and phosphorylated Mek1/2 (pMek1/2) (*C*) and total Erk1/2 and phosphorylated Erk1/2 (pErk1/2) (*D*). Quantification of immunoblots is shown on the *Right*. (*E* and *F*) Immunostaining for pErk1/2 (magenta), Nanog (yellow), and DAPI (blue, cell nuclei). White arrows indicate only pErk-positive cells; yellow arrows indicate only Nanog-positive cells; light-blue arrows indicate pErk and Nanog double-positive cells. (Scale bars, 50 μm.). (*F*) Corresponding contoured, quantitative scatter plot of imaging data. Percentages of cells in each compartment are annotated. Analysis of $n = 169$ (Scr), $n = 186$ (shM3-1), and $n = 205$ (shM3-2) cells. A representative plot is shown. a.u.: arbitrary unit. (*G*) Cells were treated with 1 μM of Mek inhibitor PD0325901 for 4 d and analyzed by flow cytometry. Proportions of Nanog^{VENUS}-negative cells are labeled. (*H*) Flow cytometry quantification of Nanog^{VENUS}-negative cells upon PD0325901 treatment over 4 d. Statistical significance was calculated using two-tailed independent *t* test with unequal variance, $*P < 0.1$, $**P < 0.05$, and $***P < 0.01$. Error bars indicate mean ± SD from (*A–D*) $n = 5$ and (*E–H*) $n = 3$ independent experiments. pMek1/2: phospho-Mek1/2(Ser217/221); and pErk1/2 (pErk): phospho-Erk1/2(Thr202/Tyr204). All experiments were performed with Nanog^{VENUS} mESCs. DMSO, dimethyl sulfoxide.

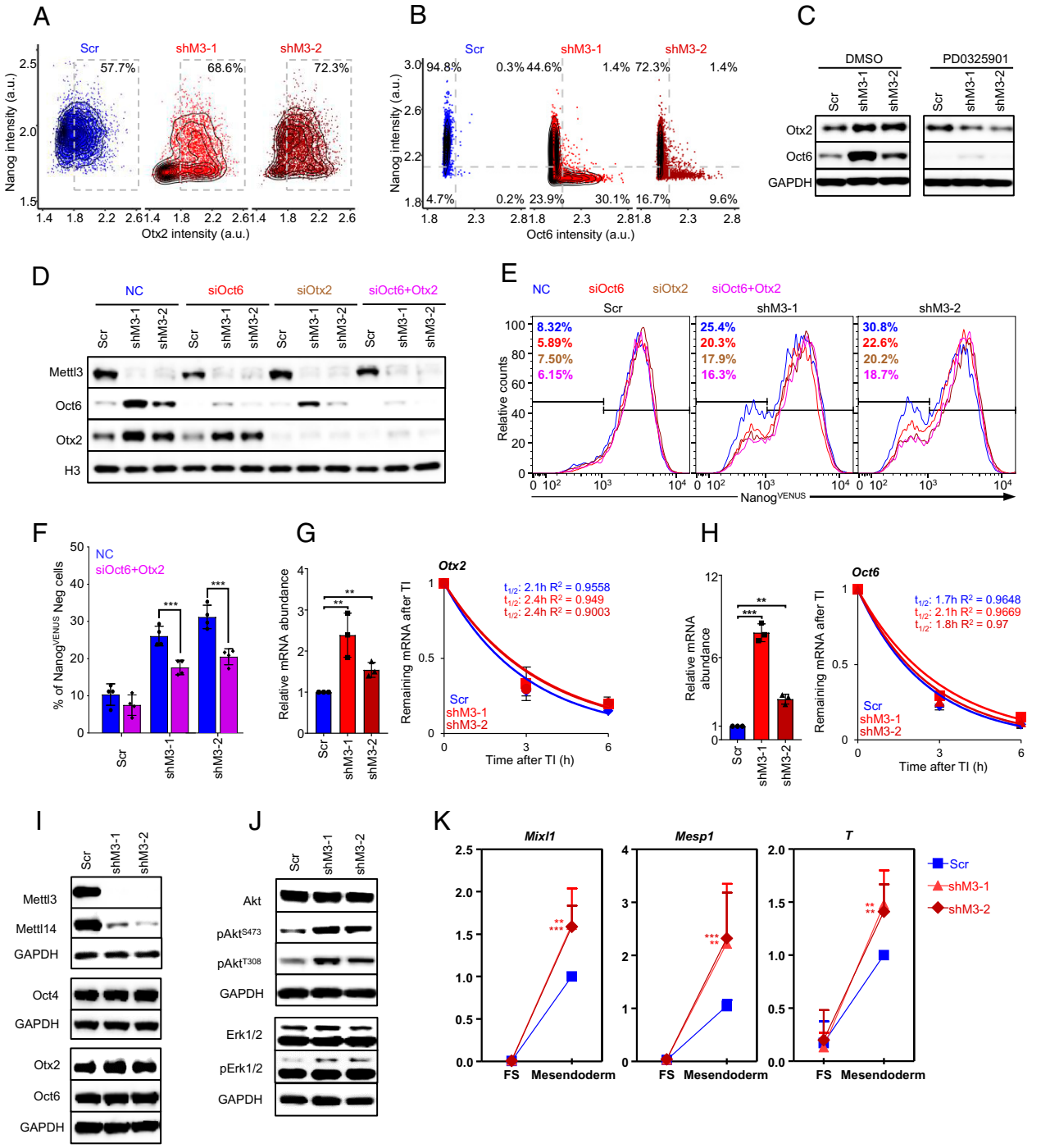

Fig. 4. m^{6}A depletion activates signaling regulating epiblast cell identity. (*A* and *B*) mESCs were transduced with control shRNA (Scr) or shRNAs targeting *Mettl3* (shM3-1 and shM3-2). Multispectral protein-level quantification of immunostaining for TFs Nanog against Otx2 n = 5,118 cells (Scr), n = 3,382 cells (shM3-1), and n = 4,326 cells (shM3-2) (*A*) and Oct6 n = 3,545 cells (Scr), n = 3,815 cells (shM3-1), and n = 6233 cells (shM-3-2) (*B*). (*A*) Dashed rectangle and percentage denotes the proportion of Otx2-positive cells. (*B*) Dashed lines separate quadrants of positive and negative cell proportions denoted by percentages. (*C*) Immunoblot analysis for Otx2 and Oct6 protein levels after Mek-pErk inhibition (PD0325901, 1 μM) or vehicle control (dimethyl sulfoxide [DMSO]). (*D*) Immunoblots showing Oct6 and/or Otx2 KD using siRNAs in m^{6}A-depleted cells. (*E*) Representative flow cytometry histograms for Nanog^{VENUS} mESCs treated with siRNA-targeting Oct6 (siOct6) and/or siOtx2 (siOtx2) in m^{6}A-depleted cells. Nanog^{VENUS}-negative cell fractions are labeled. (*F*) Quantifications of siOct6 and siOtx2 effects on Nanog^{VENUS}-negative cell fractions. (*G* and *H*) Relative mRNA levels (*Left*) and half-lives (*Right*) for *Otx2* (*G*) and Oct6 (*H*) in control and m^{6}A-depleted mESCs. Analyses were performed on Nanog^{VENUS} cells. (*I*) FS cells were induced from 2i/LIF grown R1 wild-type mESCs and cultured for 10 d. Thereafter, FS cells were transduced with Scr or shM3-1 and shM3-2 followed by m^{6}A depletion for a further 10 d in FS maintenance conditions. Immunoblot showing Mettl3, Mettl14, Oct4, Otx2, and Oct6 protein expression levels upon Mettl3 KD. (*J*) Immunoblot showing total Akt, phosphorylated Akt (pAkt^{S473}), total Erk1/2, phosphorylated Erk1/2 (pErk1/2), and GAPDH in m^{6}A-depleted FS cells. (*K*) mRNA levels quantified for mesendodermal markers *Mixl1*, *Mesp1*, and *Brachyury T*. Levels are compared in FS maintenance conditions (FS) and after 24 h of mesendodermal differentiation (Mesendoderm). The magnitude of change in gene expression is plotted relative to the mesendodermal Scr control condition delineated as 1. Error bars indicate mean ± SD from (*D*–*F*) n = 4, (*G*–*J*) n = 3, and (*K*) n = 5 independent experimental repeats. Significance is measured by two-tailed independent *t* test using unequal variance, $^{**}P < 0.05$, and $^{***}P < 0.01$. (*I*–*K*) was performed on R1 wild-type mESCs.

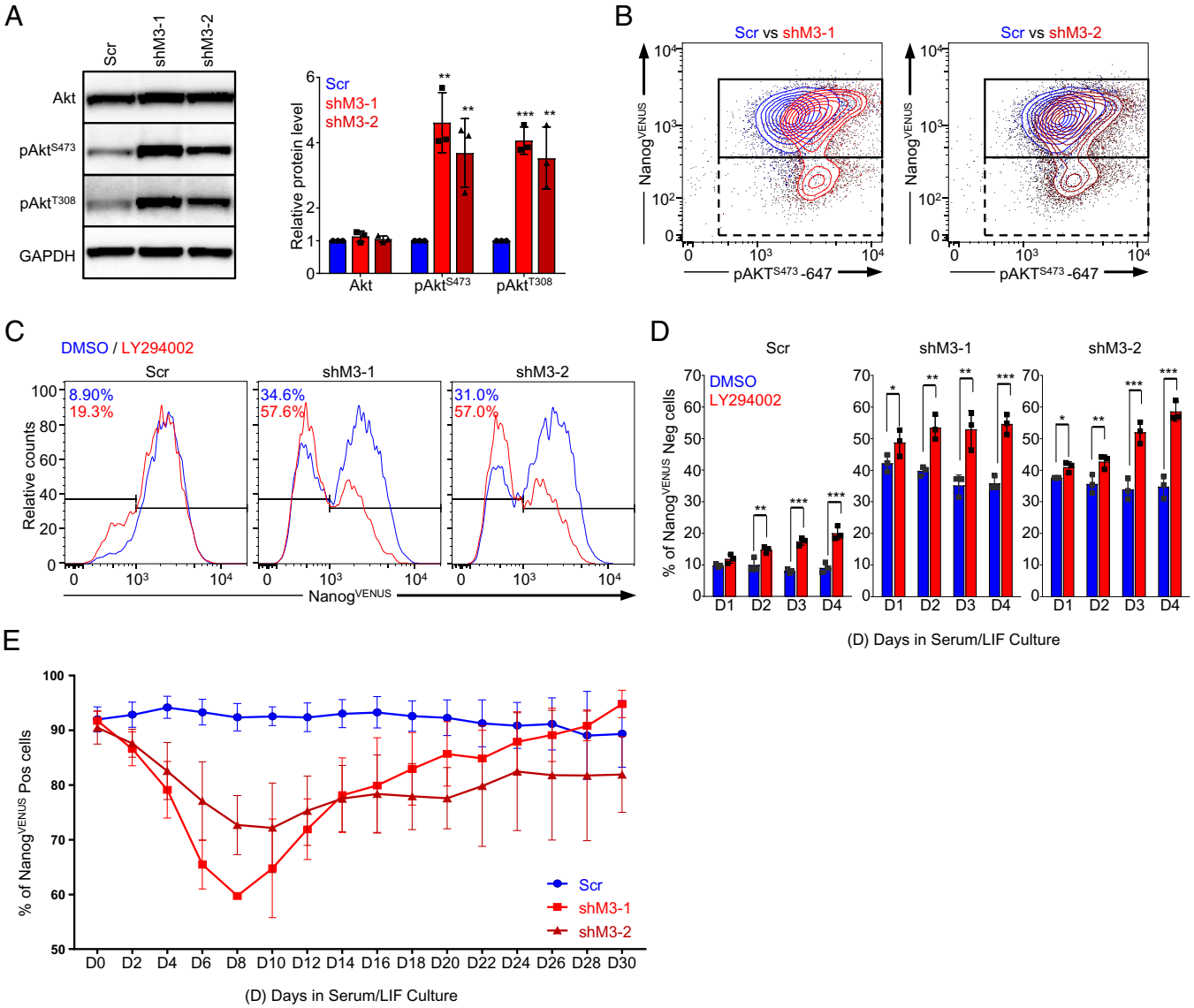

Fig. 5. m^{6}A depletion coactivates PI3K-pAkt promoting Nanog expression. (*A–E*) Nanog^{VENUS} mESCs were transduced with control shRNA (Scr) or shRNAs targeting *Mettl3* (shM3-1 and shM3-2). (*A*) Immunoblotting for total Akt and phosphorylated Akt (pAkt) on two amino acid residues, Ser473 and Thr308 (*Left*), and corresponding protein quantifications (*Right*). (*B*) Intracellular flow cytometry analysis for Alexa Fluor 647–conjugated anti-pAkt^{S473} antibody. A solid rectangle denotes the Nanog-positive population, and a dashed rectangle denotes the Nanog-negative population. Representative of $n = 5$ independent experiments. (*C*) Control and m^{6}A-depleted cells were treated with 5 μM PI3K inhibitor (LY294002) or vehicle control (dimethyl sulfoxide [DMSO]) for 4 d and analyzed by flow cytometry. Proportions of Nanog^{VENUS}-negative cells are labeled. Representative from $n = 4$ independent repeats. (*D*) Quantification of the increase in Nanog^{VENUS}-negative cell fraction upon PI3K inhibition in *C*. Statistical significance is measured by two-tailed independent *t* test with unequal variance, $*P < 0.1$, $**P < 0.05$, and $***P < 0.01$. pAkt^{S473}: phospho-Akt (Ser473); and pAkt^{T308}: phospho-Akt (Thr308). (*E*) Flow cytometry analysis was used to measure the proportions of Nanog^{VENUS}-positive cells every 2 d in Serum/LIF for a total of 30 d. All experiments shown were performed with at least three independent experimental repeats.

Results

Immediate m^{6}A Depletion Promotes Nanog-State Heterogeneity in mESCs. To observe immediate m^{6}A depletion effects, we employed short hairpin RNA (shRNA)- or small interfering RNA (siRNA)–mediated knock-down (KD) of *Mettl3* and *Mettl14* for 10 d. This significantly decreased Mettl3 and Mettl14 protein levels in mESCs (Fig. 1*A* and *SI Appendix*, Fig. 1 *A*, *C*, *E*, and *I*). Depletion of either Mettl3 or Mettl14 reciprocally down-regulates the other complex partner (Fig. 1*A* and *SI Appendix*, Fig. 1 *A*, *C*, *E*, and *I*), indicating mutual coregulation at the protein level (27, 29). *Mettl3* or *Mettl14* KD increased Wtap protein levels as previously shown (29) (Fig. 1*A* and *SI Appendix*, Fig. 1 *A*, *C*, *E*, and *I*) and reduced m^{6}A abundances on mRNA (29) (Fig. 1*B*). m^{6}A depletion resulted in a mixture of both domed, rounded, and flat, loosely formed mESC colonies (Fig. 1*C*). To determine Nanog protein levels over time in individual cells, we employed protein-fusion reporter mESCs (11). The tethering of fluorescent proteins (FPs) to the carboxy termini of TFs shows functional TF protein levels (11, 12). We confirmed no relation between the degree of m6A depletion and Nanog expression (11) (*SI Appendix*, Fig. 1 *G* and *H*). Immediate m^{6}A depletion increases the proportion of Nanog-negative cells (Fig. 1 *D* and *E* and *SI Appendix*, Fig. 1 *B*, *D*, and *F*), although almost all cells remain positive for core pluripotency TFs Oct4 and Sox2 (Fig. 1 *F*, *G*, and *H* and *SI Appendix*, Fig. 1 *J*, *K*, and *L*). Multispectral protein-level quantification showed that Oct4- and Sox2-positive, Nanog-negative cells were also negative for Klf4 (*SI Appendix*, Fig. 1*M*), Esrrb (*SI Appendix*, Fig. 1*N*), and Tbx3 (*SI Appendix*, Fig. 1*O*). The down-regulation of pluripotency TFs is accompanied by a global

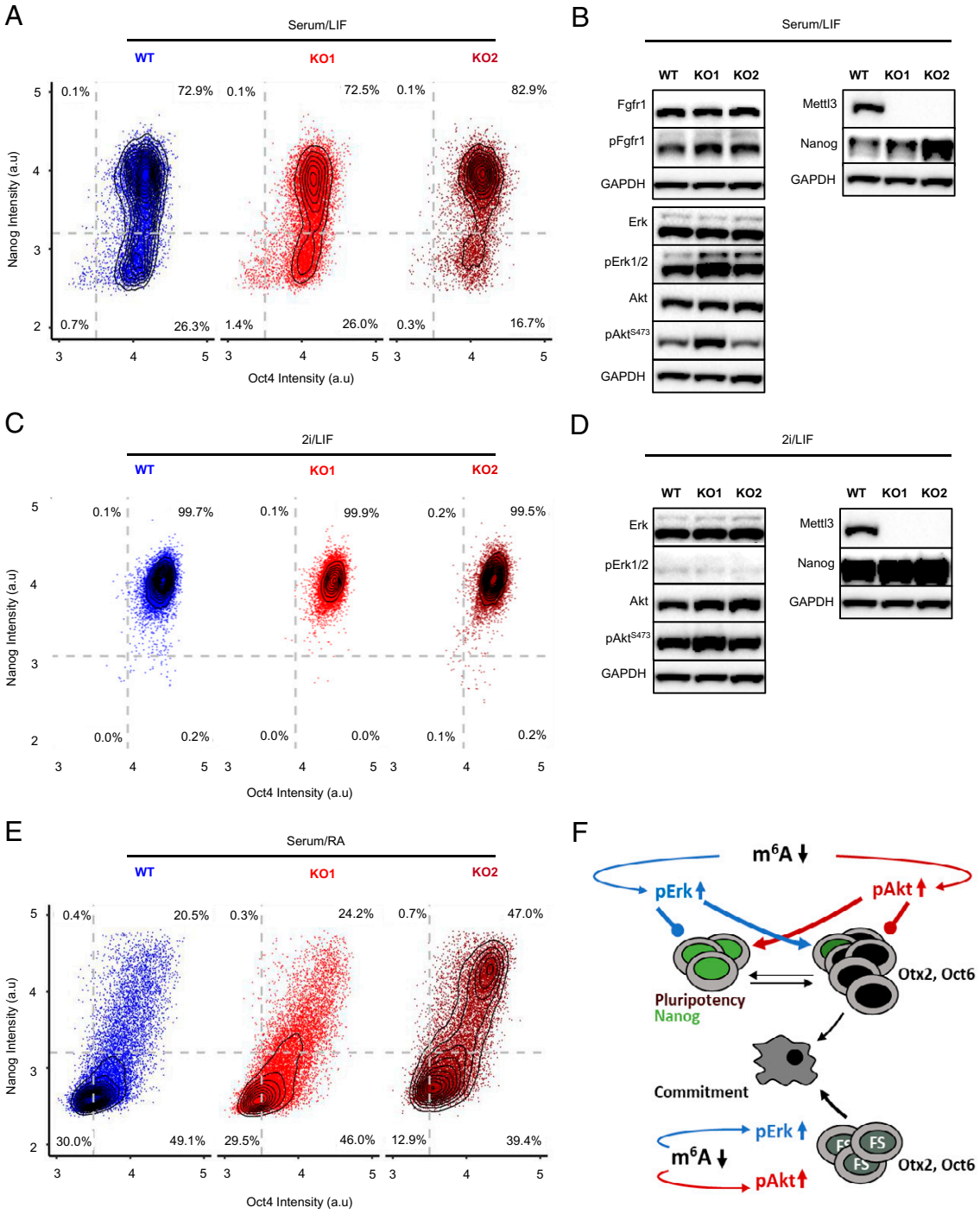

Fig. 6. Stably m^{6}A-depleted cells activate Mek-pERK facilitating pluripotency exit. (*A*–*E*) J1 wild-type (WT), Mettl3 KO clone 1 (KO1), and Mettl3 KO clone 2 (KO2) cell lines were used in experiments (*Methods*). (*A*) Multispectral, single-cell, protein-level quantification showing Nanog against Oct4 expression in Serum/LIF. WT = 10,112, KO1 = 11,399, and KO2 = 9,413 cells shown. (*B*) Immunoblotting for total FGFR1, phosphorylated FGFR1 (pFGFR1), total Akt, phosphorylated Akt (pAkt^{S473}), total Erk1/2 and phosphorylated Erk1/2 (pErk1/2), Mettl3, Nanog and GAPDH protein levels are shown. (*C*) Multispectral, single-cell, protein-level quantification showing Nanog against Oct4 expression intensity in 2i/LIF. WT = 14,215, KO1 = 13,865, and KO2 = 12,283 cells shown. (*D*) Immunoblotting for total Akt, phosphorylated Akt (pAkt^{S473}), total Erk1/2 and phosphorylated Erk1/2 (pErk1/2), Mettl3, Nanog, and GAPDH protein levels are shown. Protein levels in *B* and *D* are directly comparable, and GAPDH is used as a loading control. (*E*) Multispectral, single-cell, protein-level quantification showing Nanog against Oct4 expression intensity after 48 h of retinoic acid (RA) induced differentiation. WT = 14,445, KO1 = 14,390, and KO2 = 12,506 cells shown. (*A*–*E*) Representatives from $n = 3$ independent experimental repeats. (*F*) A model of signaling activation in m^{6}A-depleted cells. Arrows (blue or red) indicate signaling stimulation, and blunted arrows indicate inhibition of cell state, respectively. Black arrows delineate cell-state transitions, and greater thickness indicates an increase in transition propensity. In Serum/LIF, higher pErk (blue arrows) stimulates the expression of lineage TFs like Otx2 and Oct6, facilitating pluripotency exit. This is countered by increased pAkt activation (red arrows), reinforcing Nanog expression. Prolonged m^{6}A depletion may gradually strengthen the pluripotency TF network due to increased pluripotency TF mRNA stability effects. This leads to delayed pluripotency exit upon differentiation or "hyper-pluripotency." While pErk activation counteracts hyper-pluripotency in stably m^{6}A-depleted cells in Serum/LIF, pErk blockade in 2i/LIF exacerbates hyper-pluripotency. In FS cells, m^{6}A depletion activates both pAkt and pErk, tipping the signaling balance toward a state more poised for differentiation. Consequently, lineage induction in m^{6}A-depleted FS cells results in a greater propensity for mesendodermal commitment.

increase in pluripotency TF mRNA stability. This is shown by real-time PCR quantification of Nanog and Esrrb transcript abundances after 3 and 6 h of transcription inhibition with Actinomycin D (Fig. 1 *I* and *J*) (28). In comparison, no mRNA stability effects were observed for *Oct4*, which does not retain m^{6}A deposition–mediated regulation (27) (*SI Appendix*, Fig. 1*L*). These findings indicate that pluripotency TF down-regulation is disconnected from increased pluripotency TF mRNA stability observed in m^{6}A depleted cells.

m^{6}A Depletion Sustains Nanog-Positive and Negative-State Accumulation. The culture of mESCs in serum/LIF (8, 9) allows cells to undertake a reversible step toward differentiation, marked by the down-regulation of Nanog (10–12). To understand precisely how m^{6}A depletion affects this property, we sought to define the dynamics of Nanog-state heterogeneity at single-cell resolution. We created double knock-in, protein-fusion Nanog and Oct4 TF mESCs and measured protein levels continuously over many cell generations. One allele of the endogenous *Oct4* gene locus was targeted with a yellow (VENUS) FP (11), and one allele of the *Nanog* gene locus was targeted with a red (KATUSHKA) FP (Fig. 2*A*). The FPs are directly fused to the carboxy termini of TF's and thus present functionally relevant protein levels in mESCs (11, 12) (*SI Appendix*, Fig. 2 *A* and *B*). After m^{6}A depletion for 10 d, effects on Nanog^{KATUSHKA} expression were reproduced for imaging (Fig. 2*B* and *SI Appendix*, Fig. 2 *C–I*). The development of clonal colonies from single cells was monitored by microscopy (11, 12). Cells were marked by constitutive expression of infrared FP (iRFP) targeted to the nuclear membrane. Computer-assisted cell tracking and quantification of time-lapse imaging was performed (11, 37). To compensate for cell cycle–dependent fluctuations in protein intensity, a cell cycle–corrected distribution was calculated. Here, only the median of Nanog^{VENUS} intensity from the initial first three time points after a cell division was quantified. Using this unbiased approach, we generated protein intensity distributions unaffected by cell-cycle convolution (11) (Fig. 2 *C* and *D*).

Mother-to-daughter inheritance analysis showed that m^{6}A-depleted, Nanog^{KATUSHKA}-negative daughter cells are four times less likely to reacquire Nanog^{KATUSHKA} expression (Fig. 2 *D* and *E*). Nearly all daughter cells inherit similar Oct4^{VENUS} levels from their mothers (*SI Appendix*, Fig. 2*J*). Cell survival or proliferation remain unchanged (38) (*SI Appendix*, Fig. 2 *K* and *L*). Lineage-tracing reveals that m^{6}A-depleted cells inherit the Nanog^{KATUSHKA}-negative, Oct4^{VENUS}-positive state for many cell generations (Fig. 2 *F* and *G*). While on average, over six generations are required before half of the Nanog^{KATUSHKA}-negative cells re-express Nanog, control cells require less than two generations (Fig. 2 *F* and *G*). Likewise, m^{6}A-depleted, Nanog^{KATUSHKA}-negative, Oct4^{VENUS}-positive cells are supported long-term, with low probability for cell-state departure (Fig. 2*E*). While either Nanog state accumulates, low-frequency dynamic interchange between these populations (Fig. 2*E*) suggests differential and opposing regulation downstream of m^{6}A depletion. We examined whether these diverse cell-state dynamics stemmed from the activation of signaling pathways in m^{6}A-depleted cells.

m^{6}A Depletion Activates Mek-pErk Promoting Nanog-Negative State Accumulation. KEGG (Kyoto Encyclopedia of Genes and Genomes) analysis of m^{6}A sequencing (m^{6}A-seq) data indicated that mRNAs of FGF (fibroblast growth factor), MAPK (mitogen-activated protein kinase) and PI3K (Phosphoinositide 3-kinase) signaling regulators are m^{6}A modified (*SI Appendix*, Fig. 3*A*) (27). m^{6}A-depleted cells over 10 d show increased mRNA levels of *Fgf5* and *Fgf2* ligands but not Fgf4 (Fig. 3*A* and *SI Appendix*, Fig. 3 *B* and *C*). This corresponds to elevated *Fgf5* mRNA stability (Fig. 3*A*). Downstream phosphorylation of the FGFR1 receptor upon m^{6}A depletion (Fig. 3*B*) activates the Mek1/2 and Erk1/2 signaling cascade (39, 40) (Fig. 3 *C* and *D*). Multispectral, single-cell, protein-level quantification for Nanog and pErk shows that pErk activation levels are similar in Nanog-positive and -negative, m^{6}A-depleted cell populations (Fig. 3 *E* and *F* and *SI Appendix*, Fig. 3*D*). pErk activation is therefore not a by-product of the increase in the proportion of Nanog-negative cells. Strikingly, inhibition of MAPK-signaling by PD0325901 reverses the accumulation of the m^{6}A-depleted, Nanog^{VENUS}-negative cell fraction and reinstates Nanog^{VENUS} expression (Fig. 3 *G* and *H*). We recapitulated these effects on the Nanog^{VENUS} distribution by adding PD173074, a specific inhibitor of FGF receptors (20) (*SI Appendix*, Fig. 3*E*). PD173074 treatment effectively down-regulated pErk (*SI Appendix*, Fig. 3*F*). These findings show that Nanog^{VENUS}-negative cell-state accumulation is regulated by FGF-dependent Mek-pErk signaling in m^{6}A-depleted cells.

m^{6}A Depletion Activates Signaling Regulating Epiblast Cell Identity. We asked whether pErk activation in m^{6}A-depleted cells promotes the expression of key TFs involved in Nanog down-regulation. *Otx2* and *Oct6* (also known as Pou3f1) are associated with Nanog depletion in mESCs (17, 41, 42) and the peri-implantation epiblast (43–46). Multispectral, single-cell, TF protein-level quantification shows that m^{6}A depletion for 10 d is accompanied by an increase in Otx2 (Fig. 4*A* and *SI Appendix*, Fig. 4 *A* and *C*) and *Oct6* (Fig. 4*B* and *SI Appendix*, Fig. 4 *B* and *C*) expressing cells. Mek-pErk appears central to the up-regulation of these TFs as MAPK inhibition by PD0325901 (Fig. 4*C*) or the blockade of FGF receptors by PD173074 (*SI Appendix*, Fig. 4*D*) depletes Otx2 and Oct6 levels. We asked whether Otx2 and Oct6 regulate the Nanog-negative cell state by knocking-down either one or both TFs simultaneously. Otx2 and Oct6 KD significantly reduced the Nanog^{VENUS}-negative cell fraction (Fig. 4 *D–F* and *SI Appendix*, Fig. 4*E*). The increase in Otx2 and Oct6 mRNA and protein levels also appears to be independent of mRNA stability in m^{6}A-depleted cells (Fig. 4 *G* and *H*). Instead, pErk activation stimulates the up-regulation of epiblast TFs, promoting Nanog-negative cell-state accumulation.

Nanog repression is also a feature of the transient EpiLC state acquisition (19). However, in Serum/LIF conditions, epiblast identity is suppressed by the continued presence of LIF (16, 47). In FGF2-supplemented, serum-free medium used to support mEpiSCs, m^{6}A depletion led to spontaneous differentiation (29). We asked whether decreasing m^{6}A abundances also rendered the recently established FS epiblast cells more amenable to lineage commitment. FS cells are maintained by endogenous FGF activity and low nodal/activin supplementation. These cells are poised to enter mesendodermal differentiation upon increased levels of either signal or canonical Wnt (20). The FS state was induced from 2i/LIF pluripotency conditions for 10 d, followed by m^{6}A depletion for a further 10 d. Marker analysis showed that Oct4 TF protein expression was unaffected, and levels of epiblast TFs Otx2 and Oct6 also remained unaltered (Fig. 4*I*). However, we observed pErk- and pAkt-signaling activation (Fig. 4*J*), while Wnt activity remained unchanged in m^{6}A-depleted FS cells (*SI Appendix*, Fig. 4*F*). FS cultures could be expanded long-term. and profiling of mesendodermal markers showed no significant up-regulation (Fig. 4*K* and *SI Appendix*, Fig. 4*G*). However, upon lineage induction of m^{6}A-depleted cells, a significant enrichment for mesendodermal markers was found as indicated by Mesp1, Mixl1, and brachyury T at the mRNA (Fig. 4*K*) and protein levels (*SI Appendix*, Fig. 4*H*). Together, these observations indicate that m^{6}A depletion activates pErk-signaling, promoting epiblast cell identity in Serum/LIF. Upon lineage induction in m^{6}A-depleted

FS cells, pErk and pAkt coactivation appears to increase the propensity for mesendodermal differentiation.

m^{6}A Depletion Coactivates PI3K-pAkt Promoting Nanog Expression in Serum/LIF. We asked whether m^{6}A depletion also coactivates pAkt, promoting Nanog expression and pluripotency maintenance in Serum/LIF (13, 48). m^{6}A-depleted cells showed a significant increase in pAkt activation (Fig. 5*A*) spanning the Nanog protein intensity distribution (Fig. 5*B* and *SI Appendix*, Fig. 5*A*). Nanog^{VENUS}-positive cells also displayed a higher pAkt activation, consistent with its role in supporting Nanog expression. PI3K inhibition by LY294002 administration resulted in a transient Akt dephosphorylation (*SI Appendix*, Fig. 5*B*) and a significant increase in the proportion of Nanog^{VENUS}-negative cells (Fig. 5 *C* and *D*). Furthermore, inhibition of pAkt increased pErk-mediated expression of Otx2 and Oct6 (*SI Appendix*, Fig. 5*C*). pAkt can also promote pluripotency by facilitating the nuclear accumulation of β-catenin (49), resulting in Wnt pathway activation (15, 50). This is achieved by pAkt-dependent phosphorylation and degradation of the Wnt repressor Gsk3β, as also shown herein (*SI Appendix*, Fig. 5*D*). Profiling of other signaling pathways indicates that m^{6}A depletion does not affect signaling activation more broadly (*SI Appendix*, Fig. 5*E*). PI3K-pAkt and Mek-pErk regulators (51, 52) implicated in tumorigenicity (53) also remained unchanged (*SI Appendix*, Fig. 5*F*). Extended propagation in Serum/LIF reveals that the proportion of m^{6}A-depleted Nanog^{VENUS}-negative cells becomes progressively reduced over time, likely due to the increased propensity for pluripotency exit (Fig. 5*E*). Meanwhile, Nanog^{VENUS}-positive cells gradually expand in culture. These results suggest that alongside increased pluripotency TF mRNA stability (Fig. 1 *I* and *J*), pAkt activation reinforces Nanog expression in m^{6}A-depleted cells.

Stably m^{6}A-Depleted mESCs Activate Mek-pErk Facilitating Pluripotency Exit. Stable m^{6}A depletion by Mettl3 KO hampers the priming and differentiation competence of mESCs, leading to a "hyper-naıve" pluripotency phenotype. This is attributed to increased pluripotency TF mRNA stability of m^{6}A-decorated transcripts (28, 29) (*SI Appendix*, Fig. 6 *A* and *B*). We profiled Nanog and Oct4 in two KO ESC lines by multispectral, single-cell, protein-level quantification. KO1 and KO2 cell lines differ in the proportions of Oct4-positive, Nanog-negative cells in Serum/LIF (Fig. 6*A*). KO1 with a greater Oct4-positive, Nanog-negative cell fraction has higher pErk activation compared to the other cell lines. This activation threshold appears to counteract elevated pluripotency TF mRNA stability and pAkt (Fig. 6 *A* and *B*). A comparable increase in pluripotency TF mRNA stability and lower pErk activation in KO2 cells results in a reduced proportion of Nanog-negative cells in Serum/LIF (Fig. 6 *A* and *B*). Pharmacological inhibition of pErk in 2i/LIF conditions reinstates homogeneous Nanog expression (Fig. 6*C*) and increases pAkt levels in m^{6}A-depleted cells (Fig. 6*D* and *SI Appendix*, Fig. 6*C*). Induction of differentiation by retinoic acid treatment of wild-type (WT) and KO cells shows that KO1 with higher pErk activation propensity differentiates more efficiently than KO2 (Fig. 6*E*). This is characterized by a lower proportion of Oct4 and Nanog double-positive cells remaining after 48 h of retinoic acid treatment in KO1 relative to KO2. These findings show that activation of pErk-signaling in stably m^{6}A-depleted cells counteracts the pluripotency exit delay imposed by stable m^{6}A depletion.

Discussion

Decreasing m^{6}A abundances is thought to regulate fate decisions in pluripotent cells by elevating the mRNA stabilities of TFs (24, 25, 27–29, 54). Increased stability of pluripotency TF mRNAs reinforces pluripotency (28, 29) while that of lineage regulators facilitates pluripotency departure (27, 35). How cell fate is resolved upon m^{6}A depletion, however, remains poorly understood. We find that pErk- and pAkt-signaling activation in m^{6}A-depleted cells regulates pluripotent state heterogeneity and pluripotency exit propensity (Fig. 6*F*).

Immediate m^{6}A depletion by Mettl3 KD promotes Nanog-negative cell-state accumulation in Serum/LIF. This effect is disconnected from the increase in Nanog and Esrrb mRNA transcript stabilities. Instead, FGF5 ligand mRNA stability and expression facilitate FGFR1-mediated pErk activation. pErk dependent up-regulation of epiblast TFs Otx2 and Oct6 promotes Nanog down-regulation. This feature is also characteristic of the EpiLC state transition (19), although full acquisition of epiblast identity is repressed in Serum/LIF by LIF supplementation (16, 47). Interestingly, the mRNA stability of Otx2 and Oct6 is not changed by m^{6}A depletion. KD of Otx2 and Oct6 promotes the re-expression of Nanog. FGF-signaling coactivates pAkt, which also facilitates Nanog reup-regulation. pAkt further stimulates Wnt-signaling, supporting pluripotency (15). Inhibition of pAkt increases Oct4^{VENUS}-positive, Nanog^{KATUSHKA}-negative cell-state accumulation. Conversely, inhibition of pErk reduces this effect. Live, quantitative, single-cell resolution imaging shows heritable, long-term, Oct4^{VENUS}-positive, Nanog^{KATUSHKA}-negative state accumulation in m^{6}A-depleted cells. In parallel, increased Nanog mRNA stability and pAkt activation appear to facilitate the gradual expansion of the Nanog^{KATUSHKA}-positive population. Together, our findings indicate that immediate m^{6}A depletion activates differential and opposing pErk- and pAkt-signaling in Serum/LIF, promoting both pluripotency and its departure (Fig. 6*F*).

These signaling pathways also appear to be required for the maintenance of the recently defined FS epiblast cells (20). The FS population prominently expresses FGF5, a number of other FGF ligands as well as FGF receptors 1 and 2 (20). FS cells are maintained by the balance of endogenous FGF activation and low nodal/activin-signaling (20). They are poised toward differentiation and respond to increased levels of either signal or of canonical Wnt by entering the mesendodermal lineage. Inhibition of FGF receptors or downstream MEK1/2 promotes the rapid collapse of FS cultures (20). As shown here, m^{6}A depletion in FS cells results in the activation of pErk and pAkt, while Wnt-signaling remains unchanged. Interestingly, unlike mEpiSCs, which undergo spontaneous differentiation upon m^{6}A depletion (29), FS cultures can be maintained in the m^{6}A-depleted state. Upon lineage induction, however, and in line with findings in mEpiSCs (29), m^{6}A depletion promotes a greater propensity for differentiation (Fig. 6*F*). Higher pAkt- and pErk-signaling activation in m^{6}A-depleted FS cells supports a state more poised toward mesendodermal lineage commitment. While little explored, the precise tuning of m^{6}A levels may facilitate controlled and robust human stem cell lineage differentiation into more mature and functional tissues for therapies (36).

On the contrary, stably m^{6}A-depleted Mettl3 KO ESCs show a reduced capacity for differentiation or "hyper-naive" pluripotency (28, 29). This strengthening of the pluripotency TF network appears to occur due to the prolonged increase in mRNA stability of pluripotency TFs. KO cell lines also show increased albeit different levels of FGF-signaling activation in Serum/LIF. This may reflect differences in the propensity for FGF-signaling prior to m^{6}A depletion. Higher pErk activation in KO cells results in greater Nanog-state heterogeneity, and this effect can be reversed by pErk inhibition. Also, higher pErk activation propensity promotes a greater degree of pluripotency exit upon differentiation. pErk activation therefore counteracts pluripotency exit delay imposed by stable m^{6}A depletion (Fig. 6*F*). Our findings are relevant for malignant cell differentiation and complement m^{6}A abundance–dependent regulation of pAkt in cancer progression (53). pErk-signaling and pAkt-dependent stimulation of Wnt (49) upon m^{6}A depletion in mEpiSCs may contribute to the dissolution of primed pluripotency (29, 55). Finally, enhanced maintenance of m^{6}A-depleted human pluripotent stem cells (28) could

originate from mRNA stability-dependent increases in FGF-signaling. In summary, single-cell resolution approaches illustrate that decreasing m^{6}A abundances regulates pluripotency exit propensity and lineage commitment by activating pErk- and pAkt-signaling pathways. Signaling activation upon m^{6}A depletion can direct pluripotent cell-fate determination independently of TF mRNA transcript stability mechanisms.

Methods

Cell Lines. mESCs from the R1 parental line (129 substrain) were electroporated with linearized Oct4-Venus-IRES-neo targeting vector and selected with G418 (200 μg/mL, catalog no. G8168-10ML, Invitrogen). Resistant ES clones were confirmed by Southern blotting. Oct4^{VENUS} heterozygous fusion mESCs underwent a second round of electroporation with the Nanog-Katushka-2A-BSD targeting vector and were selected with Blasticidin (5 μg/mL, catalog no. A11139-02, Invitrogen). The Nanog^{VENUS} line, the parental R1 ESCs, and the E14TG2a ESCs were kindly obtained from K.A.'s laboratory (BIOTEC, Technische Universitaet Dresden). Professor Howard Y. Chang kindly provided J1 (129 substrain) Mettl3 KO cell lines (KO1 and KO2) and wild-type control cells for this study grown in Serum/LIF as previously published (28).

ESC Electroporation and Southern Blotting. Electroporation was conducted as previously described (56). Antibiotic-resistant colonies were picked, expanded in 96-well plates, and DNA was extracted by Proteinase K (0315801001, Roche) digestion and NaCl–ethanol precipitation. Genomic DNA was digested overnight with the indicated enzyme(s), separated on 0.8% agarose gels, and blotted to nylon membranes (BNAZF810S, PALL). Probes were labeled with ^{32}P by random priming (11585592001, High Prime Kit, Roche). Hybridization and washes were conducted at 65 °C.

ESC Culture. mESC lines were maintained in Fetal Bovine Serum (FBS)–containing medium and feeder-free conditions as described previously (11). Retinoic acid–induced differentiation was initiated by removal of LIF and addition of 1 μM retinoic acid (Sigma-Aldrich, R2625) 24 h after cell seeding for 2 d in FBS-containing ESC medium. For 2i/LIF ground-state conditions, mESCs were cultured on Fibronectin-coated plates or flasks (Nunc) in N2B27-based, FBS-free medium supplemented with MEK inhibitor PD0325901 (1 μM) and GSK3β inhibitor CHIR99021 (3.3 μM). In 2i/LIF, mESCs were passaged by dissociating with TrypLE (Gibco, 12605010). mESCs originally cultured in FBS-containing medium were adapted to 2i/LIF conditions for at least five passages before further experimentation. For inhibitor assays in FBS/LIF (Figs. 3–5), the following concentrations of inhibitors PD0325901 (1 μM), PD173074 (0.8 μM), or LY294002 (5 μM) were used. Thereafter, cells were collected for protein extraction followed by immunoblot analyses for designated protein targets.

FS Cell Culture. Mouse FS cells were obtained from R1 ESCs in N2B27-based 2i/LIF conditions by culturing in A_{Io}XR medium (20) for at least five passages. Briefly, A_{Io}XR media contains activin A (3 ng/mL, R&D Systems), XAV939 (2 μM, Selleck), and BMS493 (1 μM, Selleck) in N2B27 basal medium. FS cell clumps were dissociated with Accutase (A1110501, Gibco) and passaged on Fibronectin (Merck Millipore, FC010)–coated plates every 2 to 3 d. Medium was replaced daily. For mesendodermal differentiation, FS cells were dissociated, washed, and seeded on Fibronectin-coated plates in N2B27 basal medium containing 20 ng/mL activin A and 3 μM CHIR99021 (Selleck) for 24 h (20).

Viral Transduction of ESC and FS Lines. Viral transduction methodology and short hairpin RNA (shRNA) sequences obtained from the Broad Institute's The RNA interference (RNAi) Consortium are described in the *SI Appendix*.

siRNA Transfection. siRNA transfection methodology and siRNA sequences used in this study are described in the *SI Appendix*.

Immunoblot Analyses. Total proteins were extracted by radioimmunoprecipitation assay (RIPA) lysis buffer containing the protease inhibitor mixture (Sigma-Aldrich, P8340) and phosphatase inhibitor mixtures (Sigma-Aldrich, P5726; P0044). Protein concentration of the lysate was quantified with Bio-Rad Bradford (Bio-Rad, 5000006) assays. Protein samples were denatured and resolved by Bolt Bis-Tris Plus Gels (Invitrogen). Separated proteins were transferred onto nitrocellulose membranes then detected with primary antibodies against Mettl3 (Abcam ab195352), Mettl14 (Sigma-Aldrich, HPA038002), Wtap (Proteintech, 60188–1-Ig), Oct4 (Santa Cruz, sc-8628), Nanog (Abcam ab80892), Oct6 (Merck Millipore, MABN738), Otx2 (R&D systems, AF1979), GSK-3β (Cell Signaling, 9315S), pGSK3β (Ser9) (Cell Signaling, 9323S), β-catenin (Santa Cruz, sc-7199), pβ-catenin(Ser33/37/Thr41) (Cell Signaling, 9561S), Phlpp2 (Abcam, ab71973), Smad1/5/9 (Abcam, ab66737), pSmad1(Ser463/465)/Smad5(Ser463/465)/Smad9 (Ser465/467) (Cell Signaling, 13820S), Ras (Abcam, ab52939), Smad2/3 (Cell Signaling, 8685S), pSmad2(Ser465/467)/Smad3(Ser423/425) (Cell Signaling, 8828S), mTOR (Cell Signaling, 2983S), pmTOR(S2481) (Abcam, ab137133), Eras (Abcam, ab192868), Pten (Cell Signaling, 9559S), PP2A C subunit (Cell Signaling, 2038S), Akt (Cell Signaling, 4691S), pAkt(Ser473) (Cell Signaling, 4060S), pAkt(Thr308) (Cell Signaling, 13038S), c-Raf (Cell Signaling, 9422S), pc-Raf(Ser338) (Cell Signaling, 9427S), Erk1/2 (Cell Signaling, 4348S), pErk1/2 (Thr202/Tyr204) (Cell Signaling, 9101S), Mek1(Abcam, ab32091), Mek2 (Abcam, ab32517), pMek1/2 (Ser217/221) (Cell Signaling, 9154S), Fgfr1 (Abcam, ab10646), pFgfr1(Tyr653/Tyr654) (Merck Millipore, 06–1433), Histone H3 (Abcam, ab85869), and GAPDH (Abcam, ab125247). The following secondary antibodies were used: Donkey anti-mouse horseradish peroxidase (HRP) (Abcam, ab6820), donkey anti-rabbit (HRP) (Abcam, ab6802), and donkey anti-Goat (HRP) (Thermo Fisher Scientific, PA1-28664). Blots were developed by enhanced chemiluminescence (ECL) (Thermo Fisher Scientific 32209 and 34095) and scanned by a Bio-Rad ChemiDoc XRS + system.

Immunoblot Quantification. The integrated optical density (IOD) of immunoblot bands was measured by Gel-Pro analyzer software (Rockville). Generally, the IOD of target bands was firstly divided by the IOD of corresponding loading-control (for example, GAPDH) bands to normalize the sample loading-dependent variation between different lanes. Then, normalized quantification of target bands from all sample lanes were divided by the normalized value of target bands from the corresponding control sample lane. The resulting ratios were used as relative abundances of target proteins across different samples. The IOD of phosphorylated protein bands were divided by the IOD of their corresponding total-protein bands. The resulting values were used to calculate relative abundance of phosphorylated protein as previously mentioned. Each analysis for relative protein abundance was performed independently for at least three experimental repeats.

Live-Cell Multicolor Flow Cytometry. mESCs were dissociated with 0.05% trypsin (Gibco, 25300054) or TrypLE. Single-cell suspensions were obtained by resuspension of the cell pallet with phosphate-buffered saline (PBS) containing 0.5% bovine serum albumin (BSA) and filtration with a 40-μm cell strainer. All samples were run on a BD LSRFortessa cell analyzer. The blue 488-nm laser and GFP detector was used to analyze the VENUS fluorescence signal. The yellow-green 561-nm laser and PE-Cy5 detector was used to analyze KATUSHKA fluorescence signal. The red 640-nm laser and Alexa Fluro 700 detector was used to analyze iRFP713 fluorescence signal. Background signal from R1 unmodified wild-type mESCs on each channel was used to align each negative gate at 10^3 signal intensities.

Intracellular Flow Cytometry. For intracellular flow cytometry analysis, cells were dissociated and then fixed using 1.5% formaldehyde (Santa Cruz, sc-281692) for 10 min at room temperature. Fixed cells were permeabilized by resuspension in 100% methanol overnight at −20 °C. Permeabilized cells were washed twice by staining buffer (PBS with 0.5% BSA and 0.02% NaN_3) and then incubated with 10 μL of Alexa Fluor 647 conjugated mouse anti-pAkt (S473) (BD Bioscience, 560343) or 5 μL of mouse IgG1 κ Isotype Control (BD Bioscience, 557714) in 50 μL staining buffer for 60 min at 4 °C. Stained cells were washed five times with staining buffer before running on a BD LSRFortessa cell analyzer.

Fluorescence-Activated Cell Sorting. Isolation of Nanog^{VENUS} fluorescent cell subpopulations in Scr or shM3 conditions was performed on BD FACS (Fluorescence-activated cell sorting) Aria II cell sorter with a BD FacsDiva software package. In order to obtain enough cells with high purity for immunoblot analysis, we applied two rounds of sorting. The first sorting was carried out on "Yield" mode to get a preliminary enrichment of the target cell population. Preliminarily sorted cells were resorted with "Purity" Mode to attain high purity of the target cell population. The purity (more than 98%) of each sorted population was confirmed immediately after sorting. FACS analyses were performed on at least three independent experiments.

m^{6}A Dot Blot Assay. Total RNA was isolated using TRIZOL (Invitrogen, 15596026) according to the manufacturer's instructions. Polyadenylated mRNA was purified by Dynabeads mRNA Purification Kit (Invitrogen, 61006). Purified mRNA was used for m^{6}A dot blot with a Bio-Dot Apparatus. In brief, mRNA was denatured and applied to rehydrated Hybond-N$^+$ membrane (GE, RPN203B) within Bio-Dot Apparatus by gentle suction vacuum. The membrane was then cross-linked in an ultraviolet (UV) light crosslinker BLX-E254nm (Vilber, France) for 5 min, followed by baking at 80 °C for 30 min. The blotted membrane was blocked with 5% nonfat milk and incubated with primary

rabbit anti-m^6 A antibody (Synaptic Systems, 202003) and followed by secondary donkey anti-rabbit (HRP) (Abcam, ab6802). Blots were developed by ECL (Thermo Fisher Scientific 34095) and scanned by Bio-Rad ChemiDoc XRS+ system. The signal density of the dot blot experiment is quantified by Gel-Pro analyzer software (Media Cybernetics) in all experiments. The relative m^{6}A abundance was calculated as the ratio of dot intensities between shM3 and Scr. Methylene blue staining was used as RNA loading control.

qRT-PCR. qRT-PCR was used to assess the relative abundance of mRNA. Methodology and primers used for qRT-PCR are described in the *SI Appendix*.

mRNA Half-Life Assay. Control, *Mettl3* KD, or *Mettl3* KO cells were seeded in 6 cm dished at 50% confluency for 24 h. Actinomycin D (Sigma-Aldrich, A1410) was added to culture medium at 5 μg/mL for 6 h, 3 h, and 0 h before collection. The total RNA was purified and applied for RT-qPCR analysis to examine mRNA abundance. The degradation rate of RNA was estimated as previously shown (53).

Immunocytochemistry. To attain feeder-free monolayer mESC culture, cells were grown on circle glass coverslips coated with Recombinant Human E-Cadherin (25 μg/ml $^{-1}$, Primorigen, S2071-500UG) according to the manufacturer's instructions in 24-well plates for 2 d. ESCs were then rinsed briefly and fixed with 4% paraformaldehyde (Santa Cruz, sc-281692) in PBS at room temperature for 5 min. After permeabilization with PBS containing 0.25% Triton X-100 (For pErk1/2 and pStat3 staining, cells were permeabilized with ice-cold 100% methanol for 10 min at −20 °C, followed by rinse in 1× PBS for 5 min) and blocking with 5% donkey serum for 30 min, the coverslips were incubated with a primary antibody combination at optimized dilutions overnight at 4 °C. The next day, coverslips were washed with PBS four times and incubated with the secondary antibody combination at room temperature for 1 h. For triple fluorescence staining, three primary antibodies raised in different species were used, followed by compatible secondary antibodies, conjugated with fluorophores: Alexa Fluor 488, 555, or 647. Negative control-staining was done using secondary antibodies only. After secondary antibody incubation, coverslips were washed five times and counterstained with antifade Mounting medium containing DAPI (Vector Laboratories, H1200). Images of stained cells were then acquired by wide-field microscopy.

Cells seeded in 8-well μ-Slides (Ibidi, 80826) were used to estimate the correlation between FP-fusion and total-protein levels. Imaging of Nanog^{KATUSHKA} and Oct4^{VENUS} FP-fusions in live cells was first done followed by in situ immunostaining of fixed cells. Exposure time used for immunestaining yielded no fluorescence protein detection, ensuring no interference from FP-fusion signal during the imaging of immuno-stained samples. Spatial shifts in image x, y between DAPI images from staining and live-cell imaging of corresponding Nanog^{KATUSHKA} or Oct4^{VENUS} signals were realigned by manual correction using Photoshop software.

The following antibodies were used: goat anti-Oct-3/4 (Santa Cruz, sc-8628), rabbit anti-Oct3/4 (Abcam, ab19857), rabbit anti-Nanog (Abcam ab80892), mouse anti-Nanog (BD Pharmingen, 560259), mouse anti-Sox2 (Abcam, ab79351), mouse anti-Esrrb (R&D systems, PPH6705-00), mouse anti-Klf4 (Abcam, ab75486), rabbit anti-Tbx3 (gift from Prof. Hitoshi Niwa), mouse anti-Oct6 (Merck Millipore, MABN738), goat anti-Otx2 (R&D systems, AF1979), rabbit anti-pErk1/2 (Thr202/Tyr204) (Cell Signaling, 9101s), Stat3 (Cell Signaling, 12640S), pStat3(Tyr705) (Cell Signaling, 9145S), and goat anti-T (1/200, R&D, AF2085). Alexa Fluor 488–conjugated donkey anti-mouse (Invitrogen, A-21202), donkey anti-rabbit (Invitrogen, A21206), Alexa Fluor 555–conjugated donkey anti-mouse (Invitrogen, A31570), donkey anti-rabbit (Invitrogen, A31572); Alexa Fluor 647–conjugated donkey anti-mouse (Invitrogen, A31571), donkey anti-mouse (Invitrogen, A-21447) were used as secondary antibodies.

The following filters sets were used: Filter Set 38 HE (Zeiss, 489038–9901-000) for the 488-nm channel, mCherry hardcoated (HC) Filterset (AHF, F36-508) for the 555-nm channel, Cy5 ET Filterset (AHF, F46-006) for the 647-nm channel, and Filter Set 49 (Zeiss, 488049–9901-000) for the DAPI channel.

Immunofluorescence Quantification. Staining images were firstly background corrected with the BaSiC (57) package for quantitative analyses. Nuclei areas were determined and segmented according to DAPI-staining by a custom-made Fiji script. For pErk1/2-staining analysis, manual segmentation was used to determine cytoplasmic areas for quantification (*SI Appendix*, Fig. 4*L*). The intensity of fluorescence signals within segmented areas for individual cells were quantified using the program Fiji. Data processing and visualization of staining quantifications were done with RStudio (R version 3.6) and the ggplot2 package. Cells within a range of 40 to 650 px in nuclear area were analyzed to reduce segmentation artifacts. The original quantified intensities were transformed by Log10 function for final plotting.

Time-Lapse Imaging. In total, 2,000 ESCs from Scr or shM3 conditions were seeded in one well of 96-well μ-plates (Catalog no. 89626, Ibidi) coated with Recombinant Human E-Cadherin (50 μg/mL $^{-1}$, Primorigen, S2071-500UG). After seeding, plates were leveled on the microscope stage with 5% CO_2 using a self-developed continuous gas delivery lid system and cultured at 37 °C. Imaging was initiated as soon as position grids were established in each well. Imaging was conducted on previously mentioned wide-field microscope (Zeiss), with a pE-4000 CoolLED light engine, Micro-Manager Version 2.0 beta control software, Hamamatsu camera, and a 10× FLUAR objective (Zeiss). Images were acquired on live cells at 10 ms in bright-field and 250 ms for the VENUS channel using a yellow fluorescence protein (YFP) Filter Set (AHF, F46-003), 250 ms for the KATUSHKA channel using an mCherry HC Filter Set (AHF, F36-508), and 50 ms for the nuclear marker iRFP channel using a customized iRFP filter (AHF). Continuous time-lapse imaging of mESCs was conducted for a minimum of 4 d. Channels were imaged continuously at 30-min intervals per position. All experiments were performed over three independent experimental repeats.

Single-Cell Tracking. Single-cell tracking was performed as previously described (11). Briefly, tracking was done by using "the tracking tool" (TTT) program (37) on a desktop computer with 32 GB of random access memory (RAM), Quad-core central processing unit (CPU), and Windows 64-bit operating systems. Individual cells from a selected colony were identified and tracked through manually evaluating every time point of iRFP channel in a time-lapse movie. All relevant properties and behavior (division, death, and migration) of cells of interest were marked, stored, and displayed in pedigrees. All cell tracking was done manually; only cells with unequivocal identity that could clearly be identified when evaluating the video were used for analysis and all cells with questionable identity were excluded from analyses. "the tracking tool"

Background Correction and Quantification in Time-Lapse Movies. Fluorescence image normalization was done as previously described (57). Briefly, after subtracting the estimated time-dependent background and correcting uneven illumination, normalized images were used for fluorescence-intensity quantification of tracked single cells. The software package QTFy (37) was used to semiautomatically quantify the nuclear signal of tracked cells, resulting in normalized intensity time traces. Nuclei were first automatically segmented based on the nucmem-iRFP signal and further corrected manually by referring to multichannel images. Oct4^{VENUS} or Nanog^{KATUSHKA} signals were then quantified electronically from nuclear segmentation.

Cell Cycle–Corrected Protein Distribution. To compensate for cell cycle–dependent fluctuations in signal intensity, cell cycle–corrected values were used for distributions and cell-state transition analyses. To this end, only the initial Nanog^{KATUSHKA} or Oct4^{VENUS} intensities were considered (that is, median of first three time points) for each single cell. For heat-tree visualization in Fig. 2*H*, the absolute Oct4^{VENUS} or Nanog^{KATUSHKA} intensities in single-cell trajectories were cell cycle corrected by nuclear volume, as previously shown (11). The resulting intensity concentrations over the entire cell lifetime were shown in heat trees.

Negative Gate in Time-Lapse Movies. For Nanog expression, an intensity of Log10 1.4 a.u. (arbitrary units) nicely separated the bimodal Nanog^{KATUSHKA} intensity distribution in all three *Mettl3* KD experiments. For Oct4 expression, the negative gate was set to Log10 1.7 with ∼5% of Oct4^{VENUS}-negative cells being present across all three independent experiments, reflecting FACS analyses. For heat-tree visualization in (Fig. 2*H*), cells visually negative in time lapse throughout their lifetimes were quantified to determine the electronic negative gate threshold for Nanog^{KATUSHKA} and/or Oct4^{VNEUS} intensity concentrations.

KEGG Enrichment Analysis. Mettl3 and Mettl14 target gene list from the *SI Appendix*, Table 1 in Wang's publication (27) were used for KEGG pathway enrichment analysis. The KEGG enrichment analysis was done by RStudio (R version 3.6) and the cluster-Profiler package (58). Top 30 enriched pathways were shown in a dot plot in *SI Appendix*, Fig. 3*A*.

Statistics and Reproducibility. At least three independent experiments were done for each assay. Data are presented as the mean ± SD. Two-tailed Student's *t* tests assuming unequal variances were performed to assess the statistical significance of differences between groups. Pearson correlation coefficients (*r*) were calculated to assess correlation. Statistical significance (*P*) was assessed by a two-tailed *t* test of $r = 0$. Immunoblots shown are the representative images of at least three independent experiments. For box plots, the center line represents the median, the box limits show the upper and lower quartiles, whiskers represent 1.5

times the interquartile range, and outliers are represented as individual data points.

Data Availability. The following is contained in *SI Appendix*, Figs. 1–6. An immunoreagent list is supplied in *SI Appendix*, Table 1. Statistics source data for Figs. 1–6 and *SI Appendix*, Figs. 1–6 is provided in *SI Appendix*, Table 2. Unprocessed immunoblots and Southern blotting images are provided in *SI Appendix*, Fig. 7. Detailed methodology for viral transduction of ESC and FS cell lines, siRNA transfections and qRT-PCR are provided in the *SI Appendix*. Source data for quantitative imaging analyses is provided in Dataset 1. Due to size restrictions, quantitative live-cell imaging raw data pertaining to Fig. 2 *C–G* and *SI Appendix*, Fig. 2 *J–L* are available from the corresponding authors upon request.

ACKNOWLEDGMENTS. We extend gratitude to Professor Howard Chang (Stanford University) for providing us with Mettl3 KO mESCs for this study and Professor Hitoshi Niwa (Kumamoto University) for the anti-mouse Tbx3 antibody. We kindly thank the Norwegian Helse Sør-Øst funding agency, Project No. 2016053, and the Norwegian Research Council funding agency, Project Number No. 247656, for funding this research.

1. H. Niwa, J. Miyazaki, A. G. Smith, Quantitative expression of Oct-3/4 defines differentiation, dedifferentiation or self-renewal of ES cells. *Nat. Genet.* **24**, 372–376 (2000).
2. Y.-H. Loh *et al.*, The Oct4 and Nanog transcription network regulates pluripotency in mouse embryonic stem cells. *Nat. Genet.* **38**, 431–440 (2006).
3. J. Kim, J. Chu, X. Shen, J. Wang, S. H. Orkin, An extended transcriptional network for pluripotency of embryonic stem cells. *Cell* **132**, 1049–1061 (2008).
4. I. Chambers, S. R. Tomlinson, The transcriptional foundation of pluripotency. *Development* **136**, 2311–2322 (2009).
5. R. Lu *et al.*, Systems-level dynamic analyses of fate change in murine embryonic stem cells. *Nature* **462**, 358–362 (2009).
6. J. Silva *et al.*, Nanog is the gateway to the pluripotent ground state. *Cell* **138**, 722–737 (2009).
7. R. A. Young, Control of the embryonic stem cell state. *Cell* **144**, 940–954 (2011).
8. A. G. Smith *et al.*, Inhibition of pluripotential embryonic stem cell differentiation by purified polypeptides. *Nature* **336**, 688–690 (1988).
9. R. L. Williams *et al.*, Myeloid leukaemia inhibitory factor maintains the developmental potential of embryonic stem cells. *Nature* **336**, 684–687 (1988).
10. I. Chambers *et al.*, Nanog safeguards pluripotency and mediates germline development. *Nature* **450**, 1230–1234 (2007).
11. A. Filipczyk *et al.*, Network plasticity of pluripotency transcription factors in embryonic stem cells. *Nat. Cell Biol.* **17**, 1235–1246 (2015).
12. A. Filipczyk *et al.*, Biallelic expression of nanog protein in mouse embryonic stem cells. *Cell Stem Cell* **13**, 12–13 (2013).
13. H. Niwa, K. Ogawa, D. Shimosato, K. Adachi, A parallel circuit of LIF signalling pathways maintains pluripotency of mouse ES cells. *Nature* **460**, 118–122 (2009).
14. Q. L. Ying, J. Nichols, I. Chambers, A. Smith, BMP induction of Id proteins suppresses differentiation and sustains embryonic stem cell self-renewal in collaboration with STAT3. *Cell* **115**, 281–292 (2003).
15. Q.-L. Ying *et al.*, The ground state of embryonic stem cell self-renewal. *Nature* **453**, 519–523 (2008).
16. T. Boroviak, R. Loos, P. Bertone, A. Smith, J. Nichols, The ability of inner-cell-mass cells to self-renew as embryonic stem cells is acquired following epiblast specification. *Nat. Cell Biol.* **16**, 516–528 (2014).
17. T. Kalkan, A. Smith, Mapping the route from naive pluripotency to lineage specification. *Philos. Trans. R. Soc. Lond. B Biol. Sci.* **369**, 20130540 (2014).
18. A. Smith, Formative pluripotency: The executive phase in a developmental continuum. *Development* **144**, 365–373 (2017).
19. K. Hayashi, H. Ohta, K. Kurimoto, S. Aramaki, M. Saitou, Reconstitution of the mouse germ cell specification pathway in culture by pluripotent stem cells. *Cell* **146**, 519–532 (2011).
20. M. Kinoshita *et al.*, Capture of mouse and human stem cells with features of formative pluripotency. *Cell Stem Cell* **28**, 453–471.e8 (2021).
21. I. G. Brons *et al.*, Derivation of pluripotent epiblast stem cells from mammalian embryos. *Nature* **448**, 191–195 (2007).
22. Y. Kojima *et al.*, The transcriptional and functional properties of mouse epiblast stem cells resemble the anterior primitive streak. *Cell Stem Cell* **14**, 107–120 (2014).
23. A. Tsakiridis *et al.*, Distinct Wnt-driven primitive streak-like populations reflect in vivo lineage precursors. *Development* **141**, 1209–1221 (2014).
24. M. Frye, B. T. Harada, M. Behm, C. He, RNA modifications modulate gene expression during development. *Science (80-.)* **361**, 1346–1349 (2018).
25. I. A. Roundtree, M. E. Evans, T. Pan, C. He, Dynamic RNA modifications in gene expression regulation. *Cell* **169**, 1187–1200 (2017).
26. B. S. Zhao, I. A. Roundtree, C. He, Post-transcriptional gene regulation by mRNA modifications. *Nat. Rev. Mol. Cell Biol.* **18**, 31–42 (2017).
27. Y. Wang *et al.*, N6-methyladenosine modification destabilizes developmental regulators in embryonic stem cells. *Nat. Cell Biol.* **16**, 191–198 (2014).
28. P. J. Batista *et al.*, m(6)A RNA modification controls cell fate transition in mammalian embryonic stem cells. *Cell Stem Cell* **15**, 707–719 (2014).
29. S. Geula *et al.*, Stem cells. m6A mRNA methylation facilitates resolution of naïve pluripotency toward differentiation. *Science* **347**, 1002–1006 (2015).
30. J. Liu *et al.*, A METTL3-METTL14 complex mediates mammalian nuclear RNA N6-adenosine methylation. *Nat. Chem. Biol.* **10**, 93–95 (2014).
31. X.-L. Ping *et al.*, Mammalian WTAP is a regulatory subunit of the RNA N6-methyladenosine methyltransferase. *Cell Res.* **24**, 177–189 (2014).
32. G. Jia *et al.*, N6-methyladenosine in nuclear RNA is a major substrate of the obesity-associated FTO. *Nat. Chem. Biol.* **7**, 885–887 (2011).
33. G. Zheng *et al.*, ALKBH5 is a mammalian RNA demethylase that impacts RNA metabolism and mouse fertility. *Mol. Cell* **49**, 18–29 (2013).
34. B. S. Zhao, C. He, Fate by RNA methylation: m6A steers stem cell pluripotency. *Genome Biol.* **16**, 43 (2015).
35. J. Wen *et al.*, Zc3h13 regulates nuclear RNA m^6A methylation and mouse embryonic stem cell self-renewal. *Mol. Cell* **69**, 1028–1038.e6 (2018).
36. A. Klungland, J. A. Dahl, G. Greggains, P. Fedorcsak, A. Filipczyk, Reversible RNA modifications in meiosis and pluripotency. *Nat. Methods* **14**, 18–22 (2016).
37. O. Hilsenbeck *et al.*, Software tools for single-cell tracking and quantification of cellular and molecular properties. *Nat. Biotechnol.* **34**, 703–706 (2016).
38. H. Chen *et al.*, Erk signaling is indispensable for genomic stability and self-renewal of mouse embryonic stem cells. *Proc. Natl. Acad. Sci. U.S.A.* **112**, E5936–E5943 (2015).
39. A. Molotkov, P. Mazot, J. R. Brewer, R. M. Cinalli, P. Soriano, Distinct requirements for FGFR1 and FGFR2 in primitive endoderm development and exit from pluripotency. *Dev. Cell* **41**, 511–526.e4 (2017).
40. M. Kang, V. Garg, A.-K. Hadjantonakis, Lineage establishment and progression within the inner cell mass of the mouse blastocyst requires FGFR1 and FGFR2. *Dev. Cell* **41**, 496–510.e5 (2017).
41. F. Tang *et al.*, Deterministic and stochastic allele specific gene expression in single mouse blastomeres. *PLoS One* **6**, e21208 (2011).
42. M. Iwafuchi-Doi *et al.*, Transcriptional regulatory networks in epiblast cells and during anterior neural plate development as modeled in epiblast stem cells. *Development* **139**, 3926–3937 (2012).
43. D. Acampora, L. G. Di Giovannantonio, A. Simeone, Otx2 is an intrinsic determinant of the embryonic stem cell state and is required for transition to a stable epiblast stem cell condition. *Development* **140**, 43–55 (2013).
44. C. Buecker *et al.*, Reorganization of enhancer patterns in transition from naive to primed pluripotency. *Cell Stem Cell* **14**, 838–853 (2014).
45. S.-H. H. Yang *et al.*, Otx2 and Oct4 drive early enhancer activation during embryonic stem cell transition from naive pluripotency. *Cell Rep.* **7**, 1968–1981 (2014).
46. D. Acampora *et al.*, Functional antagonism between OTX2 and NANOG specifies a spectrum of heterogeneous identities in embryonic stem cells. *Stem Cell Reports* **9**, 1642–1659 (2017).
47. S.-J. Dunn, G. Martello, B. Yordanov, S. Emmott, A. G. Smith, Defining an essential transcription factor program for naïve pluripotency. *Science* **344**, 1156–1160 (2014).
48. S. Ohtsuka, Y. Nakai-Futatsugi, H. Niwa, LIF signal in mouse embryonic stem cells. *JAK-STAT* **4**, e1086520 (2015).
49. S.-N. Hassani, M. Totonchi, H. Gourabi, H. R. Schöler, H. Baharvand, Signaling roadmap modulating naive and primed pluripotency. *Stem Cells Dev.* **23**, 193–208 (2014).
50. D. ten Berge *et al.*, Embryonic stem cells require Wnt proteins to prevent differentiation to epiblast stem cells. *Nat. Cell Biol.* **13**, 1070–1075 (2011).
51. D. Meng, A. R. Frank, J. L. Jewell, mTOR signaling in stem and progenitor cells. *Development* **145**, dev152595 (2018).
52. R. A. Saxton, D. M. Sabatini, mTOR signaling in growth, metabolism, and disease. *Cell* **168**, 960–976 (2017).
53. J. Liu *et al.*, m^6A mRNA methylation regulates AKT activity to promote the proliferation and tumorigenicity of endometrial cancer. *Nat. Cell Biol.* **20**, 1074–1083 (2018).
54. A. Bertero *et al.*, The SMAD2/3 interactome reveals that TGFβ controls m^6A mRNA methylation in pluripotency. *Nature* **555**, 256–259 (2018).
55. B. Greber *et al.*, Conserved and divergent roles of FGF signaling in mouse epiblast stem cells and human embryonic stem cells. *Cell Stem Cell* **6**, 215–226 (2010).
56. K. Anastassiadis, F. Schnütgen, H. von Melchner, A. F. Stewart, Gene targeting and site-specific recombination in mouse ES cells. *Methods Enzymol.* **533**, 133–155 (2013).
57. T. Peng *et al.*, A BaSiC tool for background and shading correction of optical microscopy images. *Nat. Commun.* **8**, 14836 (2017).
58. G. Yu, L. G. Wang, Y. Han, Q. Y. He, clusterProfiler: An R package for comparing biological themes among gene clusters. *OMICS* **16**, 284–287 (2012).